PNAS
www.pnas.org

Supplementary Information for

Photoelectric conversion on Earth's surface via widespread Fe- and Mn-mineral coatings

Anhuai Lu, Yan Li, Hongrui Ding, Xiaoming Xu, Yanzhang Li, Guiping Ren, Jing Liang, Yuwei Liu, Hao Hong, Ning Chen, Shengqi Chu, Feifei Liu, Yan Li, Haoran Wang, Cong Ding, Changqiu Wang, Yong Lai, Juan Liu, Jeffrey Dick, Kaihui Liu, Michael F. Hochella Jr.

Corresponding author: Anhuai Lu, Kaihui Liu, Michael F. Hochella Jr
Email: ahlu@pku.edu.cn; khliu@pku.edu.cn; hochella@vt.edu

This PDF file includes:

www.pnas.org/cgi/doi/10.1073/pnas.1902473116

Extended Materials and Methods

Standard Sample Preparation.

The triclinic-birnessite standard sample was prepared following the improved procedure of Giovanoli in low temperature and alkali media (1, 2). The solutions, 250 mL of 0.8 M $MnSO_4$ and 250 mL of 10 M KOH were prepared and cooled below to 10 ℃. Then the solution of KOH was poured quickly into the solution of $MnSO_4$, and the air was bubbled into the solution through an air compressor. The optimal aeration rate was 30 L/min, the reaction temperature was kept below 5 ℃ and the magnetic stirring speed was controlled at 450 r/min. The oxidation reaction lasted for 5 h.

The hexagonal-birnessite standard sample was synthesized according to the OPP method at room temperature and acid media (3). The 300 mL 0.4 M $KMnO_4$ solution was heated to boiling with a controlled stirring speed of 450 r/min using a heated magnetic stirrer. Then 35 mL of 12 M HCl was added dropwise (0.7 L/min) to the $KMnO_4$ solution. After addition, the solutions were boiled for 30 min. The chemical composition of the hexagonal and triclinic birnessite was identified as $K_{0.22}Mn_{0.94}O_2$ and $K_{0.18}Mn_{1.01}O_2$, respectively, by quantifying the contents of elements though an Inductively Coupled Plasma Optical Emission Spectrometer (ICP-OES, BLUE SOP, SPECTRO, Germany).

The goethite (FeOOH) and hematite (Fe_2O_3) standard samples were purchased from Alfa Aesar Company (purity higher than 99%), and quartz and feldspar were purchased from Sinopharm Chemical Reagent Co., Ltd., China. All the other reagents used for the experiments were analytically pure, and the water for the experiments was distilled deionized water (DDW, 18 MΩ·cm).

Microscope Observation.

Polarized Optical Microscope (POM)

Thin sections were observed under a polarized optical microscope in transmission light mode. Sections were mounted on sample platforms and fixed with an attached clip. Observations were carried out under objective lenses with magnification of 5, 10 and 20 times, respectively, to select proper target areas to obtain sample morphological features.

Environmental scanning electron microscope (ESEM)

The micro-morphology and elemental composition of thin section samples were investigated by FEI Quanta 200F Environmental scanning electron microscope (School of Physics, Peking University), equipped with an energy dispersive X-ray spectrum (EDX) detector. The analysis of the elemental distribution was performed on EDX in ESEM.

Transmission electron microscope (TEM)

A drop of the suspension containing mineral powder was placed on a holey carbon film-coated TEM grid and air dried. The prepared samples were loaded into the holder of a Tecnai F20 transmission electron microscope (School of Physics, Peking University), which is equipped with an EDX detector, operating at 200 kV. The point resolution is 0.2 nm and the exposure time is 0.5 s. The acquisition time of EDX is approximately 2 min. The data were processed and analyzed using the digital micrograph software (version 3.6.5, Gantan Ltd.).

Raman Spectroscopy Analysis. Raman spectra of mineral coating powders were acquired by a Raman spectrometer (Renishaw inVia Reflex) with a laser excitation wavelength of 532 nm. Laser power was 50 mW and data were obtained with a spectral resolution of 1 cm^{-1} across the 50-1300 cm^{-1} wavenumber offset range. Experiment operation was finished under objective lens with 50 times magnification. Thirty seconds integration time for individual measurements and 10 accumulations were set to improve the signal-to-noise ratio.

X-ray Absorption Spectroscopy (XAS) Analysis. Mn *K*-edge X-ray absorption data for karst Mn coatings were collected on the Hard X-ray MicroAnalysis beamline (HXMA, 06ID) at the Canadian Light Source (4). The experiment was performed in fluorescence mode by using a Canberra 32 Ge germanium array detector. In the experiment, a Si(111) monochromator crystal and Rh mirrors (collimating and focusing mirrors) were used during data collection. The beamline monochromator was detuned to 50% of its full flux to reduce the impact from the high harmonic components in the X-ray beam; the detune energy point was set at the end of XAFS data collection energy range at 12.0 $Å^{-1}$. The monochromator energy was at first calibrated at the Mn *K*-edge by using a Mn reference

foil from the EXAFS Materials Inc., then the same reference foil was arranged between the ionization chamber detector I_1 and I_2 throughout the entire Mn experiment. Therefore, the in-step energy calibration is available for each individual scan. 100% helium gas was used in all three ionization chamber detectors during the experiment. Multiple scan data were collected from samples, and all samples were stable under the XAFS experimental conditions. The scan step-sizes used were 10 eV/step, 0.2 eV/step, and 0.05 $Å^{-1}$/step, respectively, for the pre-edge from -200 to 30 eV, XANES from -30 to 40 eV, and XAFS regions from 40 eV to 12 $Å^{-1}$ of the data range. During the data collection, the storage ring at Canadian Light Source was operated under 250 mA operation mode at 2.9 GeV, and the superconducting wiggler source of the HXMA beamline was run at 1.7 T.

The Mn-phase reference standards include: synthetic δ-MnO_2 (referring to Villalobos *et al.* (5)), β-MnO_2 (referring to Mckenzie (6)), acid birnessite (referring to Mckenzie (41)), γ-MnOOH (referring to Bochatay *et al.* (7)); and commercial Mn_2O_3 (Sigma-Aldrich), MnO (Alfa), $MnCO_3$ (Donghuan Union Chemical), and $MnSO_4$•H_2O (Xilong Chemical). The Mn *K*-edge XAFS data for these standards were collected in transmission mode by using Oxford ion chamber detectors filled with 100% He gas. The monochromatic beam was produced by using a double crystal Si(111) monochromator with the second crystal detuned by 50% at the end of the XAFS scan to reduce the high harmonic components in the X-ray beam. The beamline was configured in its focused mode with Rh mirrors (collimating and focusing mirrors) in the X-ray beam path. The in-step energy calibration was made by using a Mn metal foil set downstream to the sample. The sizes of the scan steps for the pre-edge (-200~30 eV), XANES (30~50 eV), and EXAFS (50 eV~13 $Å^{-1}$) regions were 10 eV/step, 0.25 eV/step, and 0.05 $Å^{-1}$/step respectively. During the data collection, the storage ring at Canadian Light Source was operated under 220 mA operation mode, and the superconducting wiggler source of the HXMA beamline was run at 2.2 T. Additional references are a series of calcite-rhodochrosite solid solution, $(Ca_x,Mn_{1-x})CO_3$; the Mn contents (weight percent) are 0.02%, 0.05%, 0.08% and 0.5% measured by ICP-OES, which are comparable to the Mn content measured in karst Mn coatings. The preparations were referring to Katsikopoulos *et al.* (8) And the corresponding Mn *K*-edge XAFS data were collected under fluorescence mode with the experimental settings similar to that of karst Mn coating samples, and the same scanning settings as the above Mn reference standards.

The Mn *K*-edge raw data analysis was performed using the IFEFFIT software package according to the standard data analysis procedures (9). The spectral energy of all samples was uniformly calibrated with Mn foil, thus allowing for direct comparison among the XANES of the samples. E_0 was set at the first inflection point on the absorption edge. The spectra were pre-edge background subtracted and post-edge normalized using Athena program in IFEFFIT software package. The EXAFS spectra were k^2-weighted and converted to R-space by Fourier transform over the k range of 3.3-10.8 $Å^{-1}$ using a Hanning window with *d*k set as 1 $Å^{-1}$. In Figure 1F, the Fourier transforms were not corrected for phase shifts, and the peak intensities were manually adjusted to be consistent for the first peak, in order to allow a convenient comparison for the further outer shell FT peaks. Linear combination fitting of XANES spectra of karst Mn coatings was done by Athena program in IFEFFIT using least-squares method. All of the above Mn reference standards were used as fitting components. The fitting range was from -20 to 60 eV around the edge energy. E_0 was allowed to float during fits and negative component distributions were prohibited.

Zeta Potential Measurement. All the mineral samples, synthetic hexagonal and triclinic birnessite, goethite and hematite, were crushed in a mortar and strained though 400-mesh sieve, and used to determine the zeta potential. The zeta potential measurements were performed on 1×10^{-2} g/L micron-sized powder samples, using a zeta potential measuring instrument (Brookhaven-NanoBrook). For the measurement, the samples were dissolved in 1×10^{-3} mol/L NaCl electrolyte-solution. The zeta potential was measured as a function of pH, which was controlled by adequate addition of 1×10^{-1} mol/L HCl and 1×10^{-2} mol/L NaOH or KOH.

Calculation of Photoelectric Density for Mn-rich Varnish. The solar-induced photocurrent (I_{solar}) can be calculated according to equation(1) when an average light intensity of 100 mW/cm^2 is used for calculation. When irradiated by solar light with 100 mW/cm^2 average power (AM 1.5G), the number of produced photoelectrons at per square meter (m^2) and per second (s) for Mn-rich varnish could be calculated based on equation(2).

$$I_{solar} = 3.58 \times P_{solar} = 3.58 \times 100\ nA/cm^2 = 358\ nA/cm^2 \qquad \text{Eq(1)}$$

$$n_e = \frac{I_{solar} \times t_0}{e} = \frac{358 \times 10^{-9} \times 1 \times 10^4}{1.602 \times 10^{-19}} (m^{-2} \cdot s^{-1}) = 2.23 \times 10^{16} (m^{-2} \cdot s^{-1}) \quad \text{Eq(2)}$$

In Eqs(5)-(6), I_{solar}, P_{solar}, n_e, t_0, e represent solar-induced photocurrent, solar light power, the number of photoelectrons in moles, one second and elementary charge, respectively.

Conduction and Valence Band Potential Calculation. For most semiconducting minerals, the valence band contains the highest occupied molecular orbital, while the conduction band contains the lowest unoccupied molecular orbital. Based on previous studies, the Fermi level has a Nernstian pH dependence for most metal (oxyhydr)oxides (10,11). Their band edge energy levels can be calculated using an empirical formula in the absolute vacuum scale (AVS) (12, 13), which is based on the electronegativity of the elements (10, 14, 15):

$$E_C = -\left[\chi - \frac{E_g}{2} + 0.059 \times (pH_{PZC} - pH)\right] \quad \text{Eq(3)}$$

$$E_V = E_C - E_g \quad \text{Eq(4)}$$

Where χ is the geometric mean of the electronegativity of the compound, E_g is the band gap, and pH_{PZC} is the point of zero charge.

The energy level in the electrochemical scale can be converted from the values in AVS scale:

$$E(NHE) = -E(AVS) - 4.50 \quad \text{Eq(5)}$$

For a $A_xB_yC_z$ compound, the geometric mean of the electronegativities of the constituent atoms can be expressed as:

$$\chi = \left(\chi_A^x \times \chi_B^y \times \chi_C^z\right)^{\frac{1}{(x+y+z)}} \quad \text{Eq(6)}$$

where χ_A, χ_B and χ_C are the Mulliken electronegativity (14).

The flatband potentials (U_{ft}) for metal oxides were demonstrated to be calculated with an accuracy of ~0.2 V from the atomic electronegativities of the constituent atoms (12). And the calculated band edges were within 0.5 eV of the measured flatband potential at pH_{ZPC} (U_{ft}^0) (13).

The calculated conduction band edges of hematite, goethite, hexagonal birnessite and triclinic birnessite are: 0.45 V, 0.68 V, -0.13 V and 0.09 V (vs. NHE), respectively;

and valence band edges are: 2.55 V, 3.25V, 1.69 V and 1.86 V (vs. NHE), respectively at pH=7.

Preparation of Mineral Electrodes for Aqueous Photo-electrochemical Measurements. The mineral electrodes were made by using powder samples of mineral coatings from the red soil, desert rock varnish, karst rock surface and their corresponding mineral or rock substrates, which were ground in a mortar and sieved through a 400 mesh sieve.

The mineral powder (50 mg) was mixed with anhydrous ethanol (400 μL) and Nafion (10 μL) to make the mineral paste. Then, the mineral paste was evenly smeared on a transparent conductive FTO (Fluorine-doped tin oxide, Nippon Sheet Glass Co. Ltd) substrate (16). Before use, the FTO was cleaned by sonication in acetone, ethanol, and distilled water for 30 min each. The mineral electrode was used for electrochemical measurements after drying for 12 h in air.

Photoelectrochemical Measurements. Photocurrent-time curves are used to characterize the photovoltaic response of the samples, which provide the information of the response time of photo-switching performance and photo-stability for semiconductor electrodes (16, 17). The photoelectrochemical measurements were carried out in a conventional three electrode system consisting of the mineral electrode as the working electrode, a Pt sheet as the auxiliary electrode and a SCE (saturated calomel electrode, 0.244 V *vs.* normal hydrogen electrode at 25^{o}C) reference electrode. 0.1 M Na_2SO_4 aqueous solution was used as the electrolyte. A 300 W Xe lamp (Trustech Co., China) was used as the excitation light source. The light was irradiated onto the mineral electrodes from the back face, i.e. through the quartz window, electrolyte and the FTO substrate. The incident light intensity was adjusted to 120 mW/cm^2. The photocurrent-time response of the mineral electrodes was determined by chronoamperometry with a potentiostat (CHI 660C, Shanghai Chenhua Instrument Co. Ltd, China), under a constant pre-pulsed potential of 1 V (vs. SCE), and using a hand-operated shutter to obtain light and dark response curves.

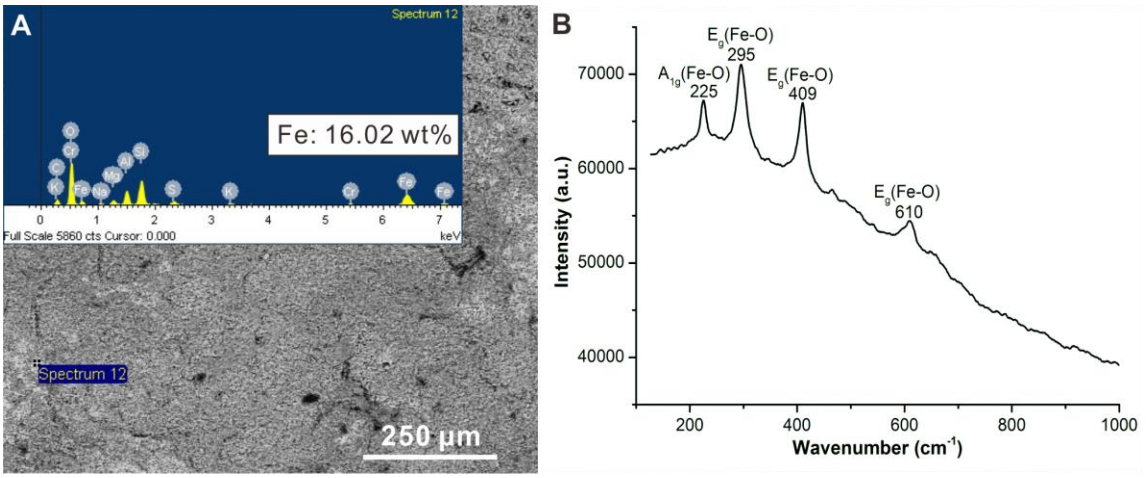

Fig. S1. Composition and structural features of the underside of Gobi rocks. (A) Back-scattered image and energy dispersive X-ray detector data (inset). (B) Raman spectrum of the regions on the underside of rocks from the Gobi region. The EDX result shows that Fe instead of Mn is the dominant element in the underside of the rock sample. The Raman spectrum shows diagnostic peaks of hematite, i.e., Fe-O symmetrical bending vibration modes at 292, 409 and 605 cm^{-1}, and Fe-O symmetrical stretching vibration mode at 226 cm^{-1}. All samples tested indicate that the Mn-rich coatings are poorly developed on the underside of the Gobi rocks.

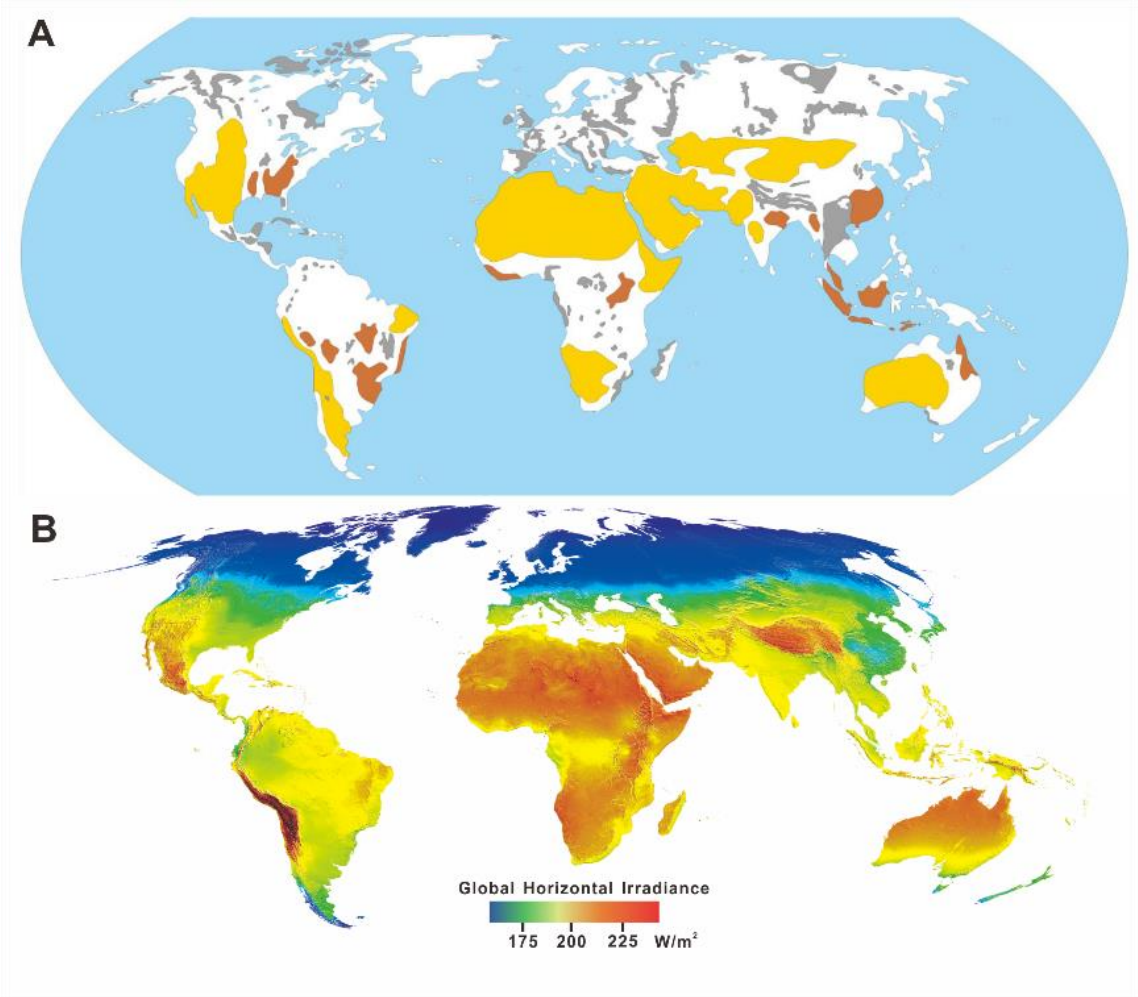

Fig. S2. Geographical comparison of the global distribution of mineral coatings and solar irradiance. (A) Schematic map showing the worldwide distribution of mineral coatings in deserts (yellow regions) (18), red soils (rust-colored regions) (19) and karst terrains (grey regions) (20). (B) Average solar irradiance (21).

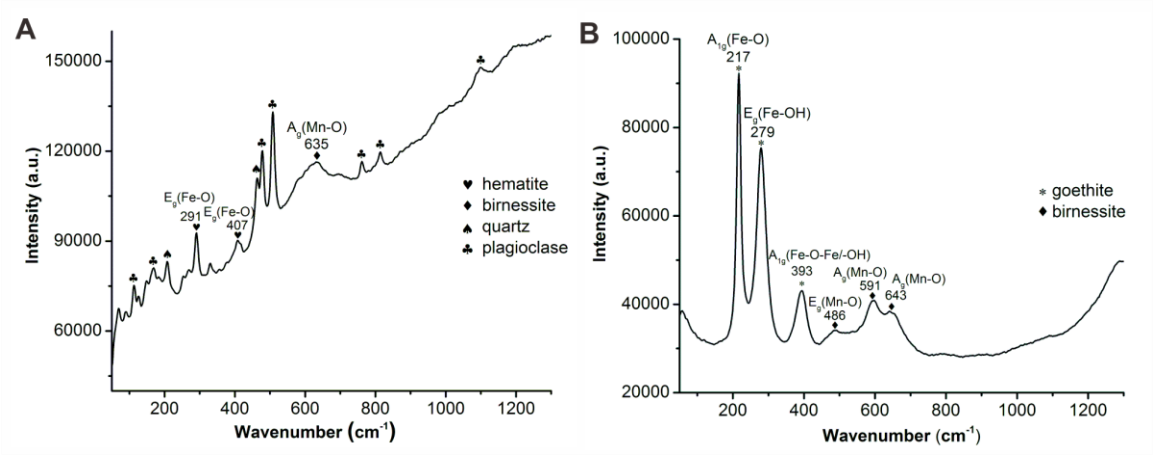

Fig. S3. (A) Raman spectrum of rock varnish on quartzite. (B) Raman spectrum of rock varnish on feldspathic quartz sandstone sample. Three types of Fe/Mn oxide minerals, i.e., hematite (291 cm^{-1} and 407 cm^{-1}), goethite (217 cm^{-1}, 279 cm^{-1} and 393 cm^{-1}) and birnessite (486 cm^{-1}, 591 cm^{-1} and 635-643 cm^{-1}) can be identified in the Raman spectra.

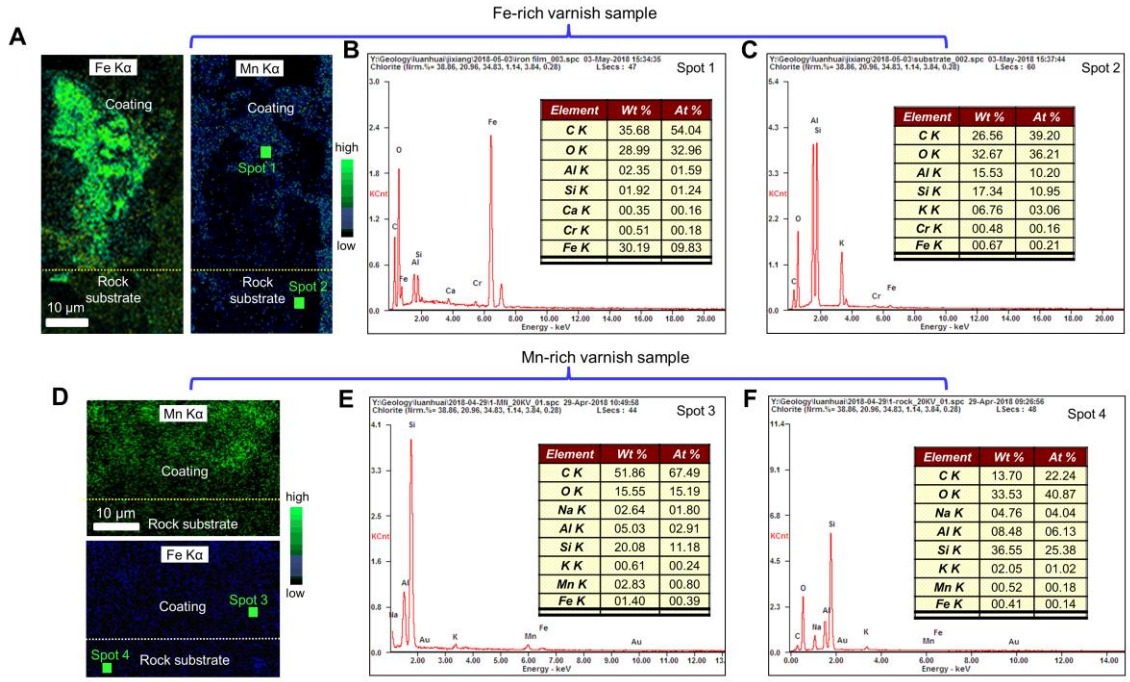

Fig. S4. EDX elemental distribution features of Fe-rich and Mn-rich desert varnish samples, respectively. (A) EDX elemental distribution patterns of a Fe-rich desert vanish thin section. (B) EDX composition and pattern of randomly selected spot 1 in panel (A). (C) EDX composition and pattern of randomly selected spot 2 in panel (A). (D) EDX elemental distribution patterns of a Mn-rich desert vanish thin section. (E) EDX composition and pattern of randomly selected spot 3 in panel (D). (F) EDX composition and pattern of randomly selected spot 4 in panel (D). The EDX results show that the content of Mn is as low as the background value in the coating of a Fe-rich varnish sample, and the content of Fe is extremely low in the coating of a Mn-rich varnish sample.

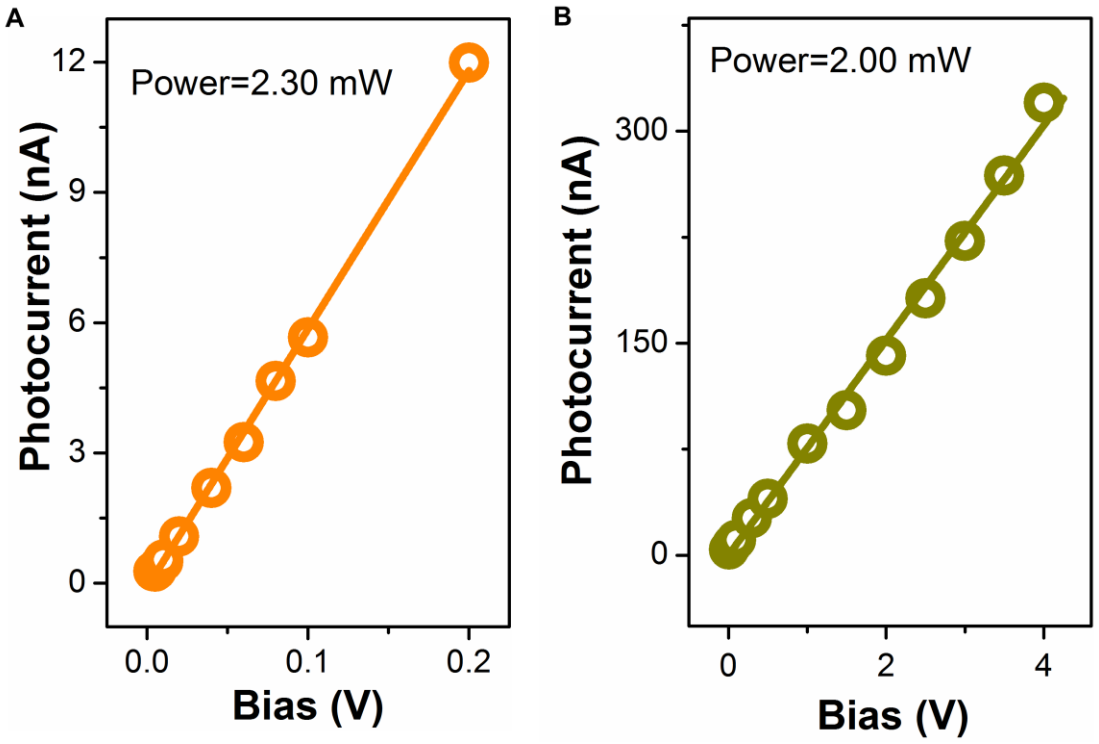

Fig. S5. Close linear relationships between *in situ* photocurrents and bias at fixed laser power. (A) Result of Fe-rich desert varnish sample, R^2=0.9988. (B) Result of Mn-rich desert varnish sample, R^2=0.9955.

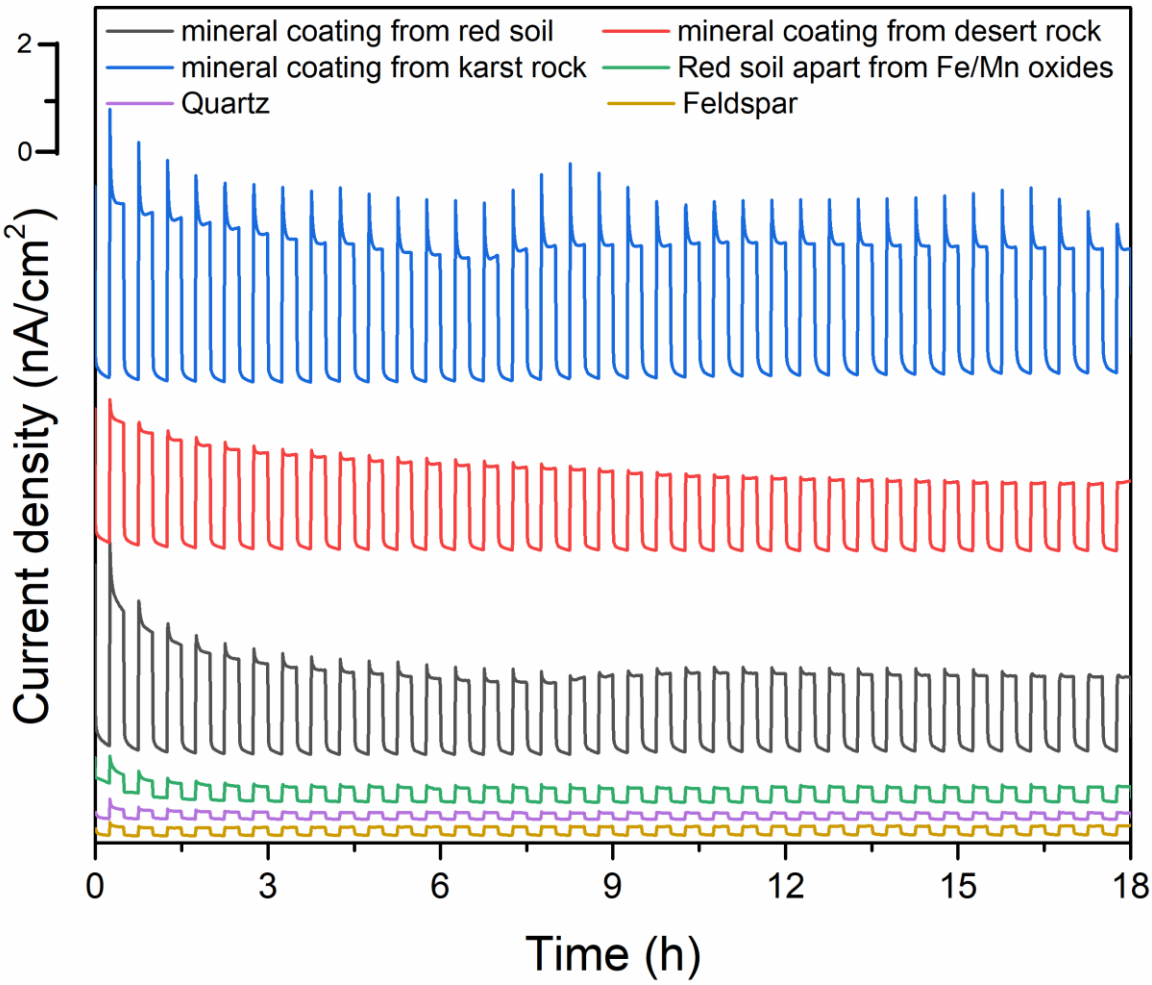

Fig. S6. Curves of current vs. time of Fe and Mn (oxyhydr)oxide "mineral coatings" as well as other minerals in the rock substrate. Photocurrent-time curves of Fe and Mn (oxyhydr)oxide mineral coatings are fixed to graphite electrodes in supporting electrolyte of 0.1 M Na_2SO_4 under simulated solar light irradiation (Xenon light source) and with an applied external bias of 1.0 V (vs. SCE). In this system, the electron donors are H_2O in the anodic chamber, while the electron acceptors are oxygen in the cathodic chamber. Similar to non-semiconducting minerals such as quartz and feldspar, the remnants apart from Fe/Mn oxides from red soil show indistinctive photo-response to the light with the current values approaching the baseline value.

References

1. Feng XH, Liu F, Tan WF, Liu XW (2004) Synthesis of birnessite from the oxidation of Mn^{2+} by O_2 in alkali medium: Effects of synthesis conditions. *Clay Clay Miner.* 52:240-250.
2. Giovanoli R (1980) *On Natural and Synthetic Manganese Nodules* (Publishing House of the Hungarian Academy of Science, Budapest, Hungary).
3. Feng XH (2004) *Syntheses, Transformations and Surface Chemistry Characteristics of the Common Manganese Oxide Minerals in Soil* (Huazhong Agricultural University Press, Wuhan, P. R. China).
4. Jiang DT, Chen N, Sheng W (2007) Wiggler-base Hard X-ray Spectroscopy Beamline at CLS. *AIP Conf. Proc.* 879:800-803.

5. Villalobos M, Toner B, Bargar J, Sposito G (2003) Characterization of the manganese oxide produced by *Pseudomonas putida* strain MnB1. *Geochim. Cosmochim. Ac.* 67:2649-2662.
6. Mckenzie RM (1971) The synthesis of birnessite, cryptomelane, and some other oxides and hydroxides of manganese. *Mineral. Mag.* 38:493-502.
7. Bochatay L, Persson P, Sjöberg S (2000) Metal ion coordination at the water–manganite (γ-MnOOH) interface: I. An EXAFS study of cadmium (II). *J. Colloid Interf. Sci.* 229:584-592 (2000).
8. Katsikopoulos D, Fernández-González Á, Prieto M (2009) Precipitation and mixing properties of the "disordered" (Mn, Ca) CO_3 solid solution. *Geochim. Cosmochim. Ac.* 73:6147-6161.
9. Newville M (2001) IFEFFIT: interactive XAFS analysis and FEFF fitting. *J. Synchrotron Radiat.* 8:322-324.
10. Butler MA, Ginley DS (1978) Temperature dependence of flatband potentials at semiconductor–electrolyte interfaces. *Nature* 273:524-525.
11. Matsumoto Y, Yoshikawa T, Sato E (1989) Dependence of the Band Bending of the Oxide Semiconductors on pH. *J. Electrochem. Soc.* 136:1389-1391.
12. Butler MA, Ginley DS (1978) Prediction of flatband potentials at semiconductor-electrolyte interfaces from atomic electronegativities. *J. Electrochem. Soc.* 125: 228-232.
13. Xu Y, Schoonen M (2000) The absolute energy positions of conduction and valence bands of selected semiconducting minerals. *Am. Mineral.* 85:543-556.
14. El Halouani F, Deschanvres A (1982) Interfaces semi-conducteur-electrolyte: correlations entre le potentiel de bande plate et les echelles d'electronegativite. *Mater. Res. Bull.* 17:1045-1052.
15. Huheey JE (1972) *Inorganic Chemistry: Principles of Structure and Reactivity (2nd Edition)* (Harper and Row, New York, USA).
16. Cheng C, Ren W, Zhang H (2014) 3D TiO_2/SnO_2 hierarchically branched nanowires on transparent FTO substrate as photoanode for efficient water splitting. *Nano Energy* 5:132-138.
17. Cho IS, et al. (2013) Codoping titanium dioxide nanowires with tungsten and carbon for enhanced photoelectrochemical performance. *Nat. Commun.* 4:1723.
18. Walker AS (1996) Deserts: Geology and Resources (University of Michigan Library, Michigan, USA).
19. Steila D, Pond TE (1989) *The Geography of Soils: Formation, Distribution, and Management (2nd Edition)* (Rowman & Littlefield Publishers, Washington DC, USA).
20. Lace MJ, Mylroie JE (2013) *Coastal Karst Landforms* (Springer, Berlin, Germany).
21. Free Wind and Solar Resource Maps (2015) http://www.vaisala.com/en/energy/support/Resources/Pages/Free-Wind-And-Solar-Resource-Maps.aspx.